Energy & Environmental Science

ROYAL SOCIETY OF CHEMISTRY

PAPER

View Article Online
View Journal | View Issue

Cite this: *Energy Environ. Sci.*, 2025, **18**, 1847

Surpassing 90% Shockley–Queisser V_{OC} limit in 1.79 eV wide-bandgap perovskite solar cells using bromine-substituted self-assembled monolayers†

Zhouyin Wei, ‡[ab] Qilin Zhou,‡[ac] Xiuxiu Niu,[ac] Shunchang Liu,[a] Zijing Dong,[ac] Haoming Liang,[ac] Jinxi Chen,[ac] Zhuojie Shi,[acd] Xi Wang,[ac] Zhenrong Jia,[ac] Xiao Guo,[ac] Renjun Guo,§[a] Xin Meng,[acd] Yu-Duan Wang,[ac] Nengxu Li,[ac] Zhiguang Xu,[e] Zaifang Li,[e] Armin Gerhard Aberle,[ab] Xinxing Yin *[e] and Yi Hou *[ac]

Received 5th September 2024,
Accepted 23rd December 2024

DOI: 10.1039/d4ee04029e

rsc.li/ees

All-perovskite tandem solar cells (TSCs) hold the promise of surpassing the efficiency limits of single-junction solar cells. However, enhancing TSC efficiency faces the challenge of significant open-circuit voltage (V_{OC}) loss in the wide-bandgap (WBG) subcell. In this study, we employed a bromine-substitution strategy to develop a novel self-assembled monolayer, (4-(3,11-dibromo-7*H*-dibenzo[*c*,*g*]carbazol-7-yl)butyl)phosphonic acid (**DCB-Br-2**), as the hole-transporting layer for 1.79-eV WBG perovskite solar cells. The bromine in **DCB-Br-2** donates a pair of non-bonded electrons to uncoordinated Pb^{2+} ions or halide vacancies, enhancing interaction with the perovskite layer and suppressing interfacial non-radiative recombination. **DCB-Br-2** also adjusts energy level alignment, facilitating fast hole extraction. The optimized WBG solar cell achieved a maximum V_{OC} of 1.37 V, surpassing 90% of the Shockley–Queisser limit. Combined with a 1.25-eV narrow-bandgap subcell, this enabled a two-terminal all-perovskite TSC with a champion power conversion efficiency of 27.70%, advancing the development of high-performance tandem devices.

Broader context

All-perovskite tandem solar cells (TSCs) have garnered significant attention due to their great potential to break the Shockley–Queisser (S–Q) limit of single-junction solar cells. However, wide-bandgap (WBG) perovskite subcells experience substantial V_{OC} loss primarily due to perovskite bulk quality, interfacial non-radiative recombination loss, and energy level misalignment, impeding the further improvement of TSCs. Recently, self-assembled monolayers (SAMs) as hole transporting layers (HTLs) have shown great promise in addressing these challenges owing to their tunable energy levels, cost-effectiveness, rapid hole extraction, and facile synthesis. Herein, we adopted a bromide-substitution strategy to modify the terminal group of the SAM. This approach effectively modulates the interfacial interaction and energy level alignment between the SAM and perovskite, resulting in reduced non-radiative recombination and faster hole extraction. Consequently, we achieved a remarkable V_{OC} of 1.37 V in a 1.79-eV WBG cell with only a 0.42 V V_{OC} loss, surpassing 90% of the S–Q V_{OC} limit. This research underscores the importance of the rational design of SAM HTLs for WBG subcells with high V_{OC}, contributing to the further advancement of high-performance TSCs.

Introduction

Perovskite solar cells (PSCs) have obtained significant attention in recent years, achieving a notable power conversion efficiency (PCE) of 26.7%,[1] approaching the theoretical limit for single-junction solar cells of approximately 33%.[2] All-perovskite tandem solar cells (TSCs) hold the potential to break the Shockley–Queisser (S–Q) limit of single-junction solar cells, boasting a higher theoretical limit of 45%.[3] The highest certified PCE of all-perovskite TSCs has reached 30.1%,[1] exceeding that of single-junction PSCs. Notably, the rapid increase in the PCE of all-perovskite TSCs is attributed to the advancements in narrow-bandgap (NBG, 1.2–1.3 eV) subcells. However,

[a] *Solar Energy Research Institute of Singapore (SERIS), National University of Singapore, Singapore, 117574, Singapore. E-mail: yi.hou@nus.edu.sg*
[b] *Department of Electrical and Computer Engineering, National University of Singapore, Singapore, 117583, Singapore*
[c] *Department of Chemical and Biomolecular Engineering, National University of Singapore, Singapore, 117585, Singapore*
[d] *Joint School of National University of Singapore and Tianjin University, International Campus of Tianjin University Fuzhou, Fuzhou, 350207, China*
[e] *China-Australia Institute for Advanced Materials and Manufacturing (IAMM), Jiaxing University, Jiaxing 314001, China. E-mail: xxyin@zjxu.edu.cn*

† Electronic supplementary information (ESI) available. See DOI: https://doi.org/10.1039/d4ee04029e

‡ These authors contributed equally.

§ Present address: Institute of Microstructure Technology, Karlsruhe Institute of Technology, Eggenstein-Leopoldshafen, 76344, Germany.

wide-bandgap (WBG, 1.7–1.8 eV) subcells suffer from larger open-circuit voltage (V_{OC}) losses than their normal-bandgap and NBG counterparts, impeding further improvement in high-efficiency all-perovskite TSCs.[4–7] The significant V_{OC} loss in WBG subcells can be attributed to bulk quality of WBG perovskites,[8–11] interfacial non-radiative recombination,[12–15] and energy level misalignment between WBG perovskites and the charge transport layer.[14–18] The design of hole-transporting layers (HTLs) plays a critical role in addressing these issues.

The most widely used HTLs in p–i–n inverted PSCs are poly[bis(4-phenyl) (2,4,6-trime-thylphenyl) amine] (PTAA) and NiO_X. However, PTAA exhibits poor wettability, while NiO_X suffers from surface defects and energy band misalignment, both requiring additional treatment to achieve high-performance WBG PSCs.[19–23] Recently, self-assembled monolayers (SAMs) have drawn attention to replacing the conventional HTLs in WBG PSCs, attributing to their tunable energy levels, improved hole selection and extraction, and reduced interfacial trap density.[7,12,24–29] SAMs typically consist of three components: anchoring groups, spacer groups, and terminal groups, offering large design potential to suit various interfaces.[26,30] For example, Zhang *et al.* modified the commonly used anchoring group phosphonic acid (–PO_3H) by adding an adjacent cyano group, forming the cyanovinyl phosphonic acid (–CPA) anchoring group with enhanced hydrophilicity.[31] Their novel SAM, MPA-CPA, featured a super-wetting HTL surface, facilitating the deposition of pinhole-free and homogeneous perovskite (PVSK) films. He *et al.* introduced a novel carbazole-derived terminal group, 7*H*-dibenzo carbazole (DCB), to form a new SAM (4-(7*H*-dibenzo[*c*,*g*]carbazol-7-yl)butyl) phosphonic acid (4PADCB).[12] DCB introduced a special steric hindrance, leading to a more homogeneous anchoring on ITO. Compared to the commercial 4PACz, 4PADCB achieved more uniform coverage and better wettability, benefiting the deposition of high-quality perovskite films. These improvements reduced non-radiative recombination loss and achieved a better device performance. Li *et al.* replaced the widely used alkyl spacer group with a conjugated phenyl spacer. Compared to MeO-2PACz, their newly designed MeO-PhPACz achieved better energy level alignment with the perovskite layer because the phenyl spacer exhibited a higher negative charge, which shifted down the work function (WF) of ITO.[32] Yi *et al.* introduced electron-withdrawing bromine (Br) substituents at the DCB terminal group to form (4-(5,9-dibromo-7*H*-dibenzo[*c*,*g*]carbazol-7-yl)butyl)phosphonic acid (DCB-BPA). The Br-substitution can lower the highest occupied molecular orbital (HOMO) level and achieve better energy level alignment, leading to a higher V_{OC}.[16] So far, most of the SAM designs have focused on improving SAM morphology,[33–35] modulating SAM surface wettability,[7,36,37] and achieving better energy level alignment.[38–40] Additionally, some studies have explored strengthening the interaction between the SAM and the perovskite layer by incorporating an interlayer between the SAM and perovskite or modifying the SAM's terminal group.[41,42] However, detailed investigations into the nature of SAM-perovskite interaction and its impact on device performance remain limited.

In this work, we focused on enhancing the interaction between SAM and perovskites by modifying the terminal group of the SAM. We introduced Br substituents to the DCB terminal group of the referenced SAM (4-(7*H*-dibenzo[*c*,*g*]carbazol-7-yl)-butyl)phosphonic acid (**DCB-C4POH**) and studied the influence of different substitution positions. The modified SAMs, (4-(5,9-dibromo-7*H*-dibenzo[*c*,*g*]carbazol-7-yl)butyl)phosphonic acid and (4-(3,11-dibromo-7*H*-dibenzo[*c*,*g*]carbazol-7-yl)butyl)phosphonic acid, are denoted as **DCB-Br-1** and **DCB-Br-2**, respectively. X-ray photoelectron spectroscopy (XPS) results demonstrated that the Br substitution position directly influences the strength of the interaction between the corresponding SAM and perovskites. **DCB-Br-2** passivates defects and suppresses non-radiative recombination more effectively due to its stronger interaction with perovskites. Additionally, it exhibits better energy level alignment, facilitating faster hole extraction. Consequently, we achieved a notable high V_{OC} of 1.37 V in a 1.79-eV WBG PSC based on **DCB-Br-2**, marking one of the highest reported V_{OC} values to date. This advancement enables the fabrication of all-perovskite TSCs with a champion efficiency of 27.70% with good operational stability, maintaining 80% of their initial PCE after 440 hours continuous operation under 1-sun illumination.

Results and discussion

The properties of SAMs

Fig. 1a–c show the chemical structure of the three studied SAMs, namely **DCB-C4POH**, **DCB-Br-1**, and **DCB-Br-2**. The detailed synthesis and characterization of **DCB-Br-2** are described in Scheme S1 and Fig. S1–S5 (ESI†). All three molecules are based on the same terminal group DCB, differing in the positioning of two Br substituents. Specifically, **DCB-C4POH** serves as the referenced SAM, with Br substituents introduced at the 5,9-position of DCB for **DCB-Br-1** (side position), and 3,11-position for **DCB-Br-2** (top position). We first investigated the morphology and optical properties of these three SAMs on ITO. The root-mean-square (RMS) roughness of ITO/SAMs slightly decreased in the order of **DCB-C4POH** (1.9 nm), **DCB-Br-1** (1 nm), and **DCB-Br-2** (0.5 nm), as observed from the atomic force microscopy (AFM) measurements in Fig. S6 (ESI†). **DCB-Br-2** performed the most uniform HTL coating, which might benefit the subsequent deposition of the perovskite layer. We then analyzed the optical properties of the SAMs using ultraviolet-visible (UV-vis) transmittance spectroscopy (Fig. S7, ESI†). The ultra-thin SAM-modified ITO exhibits high transmittance across almost the entire visible region, except for the range of 320 nm to 450 nm, which shows lower transmittance. **DCB-Br-2** exhibits slightly higher transmittance compared to **DCB-C4POH** and **DCB-Br-1**, which could potentially contribute to a higher short-circuit current (J_{SC}).

Interaction between SAMs and perovskite

Considering the high electronegative Br groups function as Lewis bases, capable of donating a pair of non-bounded electrons to uncoordinated Pb^{2+} ions or halide vacancies,[43] we conducted XPS measurements to evaluate the interaction between the Br from SAMs and Pb from perovskite. Fig. 1d and e show Br 3d spectra of ITO/SAMs and ITO/SAMs/PbI_2.

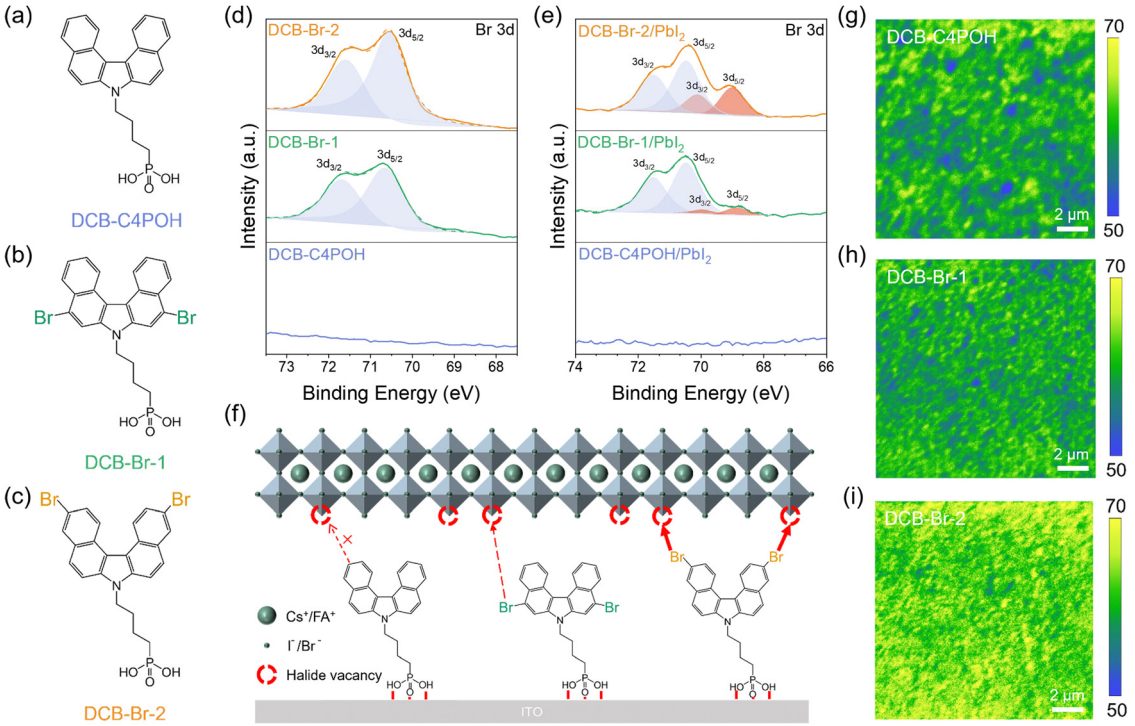

Fig. 1 Molecular structure and the interaction between SAMs and perovskite. Molecular structures of **DCB-C4POH** (a), **DCB-Br-1** (b), and **DCB-Br-2** (c). (d) XPS spectra of Br 3d of SAMs coated on ITO substrates. (e) XPS spectra of Br 3d of ITO/SAMs/PbI_2. The samples are prepared by evaporating a 5 nm PbI_2 thin film on ITO/SAMs substrates. (f) Schematic of the interaction between SAMs and the perovskite layer. Confocal PL mapping of perovskite films deposited on ITO/**DCB-C4POH** (g), ITO/**DCB-Br-1** (h), and ITO/**DCB-Br-2** substrates (i).

Comparing these two spectra with and without PbI_2, there is an obvious additional doublet with lower binding energy in the ITO/**DCB-Br-2**/PbI_2 case and a less pronounced one in the ITO/**DCB-Br-1**/PbI_2 case, which could be attributed to the Pb–Br interaction.[44–46] Furthermore, the Pb 4f peaks show a reduction in binding energy, following the order of **DCB-C4POH** (143.9 eV), **DCB-Br-1** (143.7 eV), and **DCB-Br-2** (143.6 eV) in Fig. S8 (ESI†), confirming the interaction between Br substituents and Pb atoms.[47] **DCB-Br-2** demonstrates a notably stronger interaction compared to **DCB-Br-1** due to higher electron density as shown in calculated electrostatic surface potential (ESP) results (Fig. S9, ESI†). These findings suggest that Br-substitution within the DCB terminal group exerts an obvious interaction with uncoordinated Pb^{2+} at the HTL/perovskite interface, especially for **DCB-Br-2** with smaller steric hindrance and higher electron density.[48,49] Accordingly, we drew a schematic diagram to illustrate the interaction between SAMs and perovskite (Fig. 1f).

We then investigated the morphology and crystal quality of the perovskite film based on different SAMs with various interactions. The **DCB-Br-2**-based perovskite film exhibits a slightly larger grain size without pinholes compared with the other two samples from the scanning electron microscopy (SEM) results in Fig. S10 (ESI†), which is attributed to lower nucleation density on the more hydrophobic surface of **DCB-Br-2** as shown in Fig. S11 (ESI†).[34,50] The cross-sectional SEM images of **DCB-Br-2** reveals that the perovskite bottom surface is uniform and pinhole-free. These results suggest that **DCB-Br-2** effectively enhances the bulk quality of the perovskite. The X-ray diffraction (XRD) results in Fig. S12 (ESI†) demonstrate negligible differences in perovskite crystallinity across the various SAMs. To evaluate the defect behavior of the perovskite films with different interactions with SAMs, we conducted the confocal photoluminescence (PL) mapping as shown in Fig. 1g–i and Fig. S13 (ESI†). The **DCB-Br-2**-based sample performs higher PL intensity and better uniformity due to its stronger interaction with uncoordinated Pb^{2+}, which effectively inhibits non-radiative recombination. Therefore, we demonstrate that the Br-substitution on the DCB terminal group with appropriate steric hindrance could effectively modify the halide vacancies, thereby reducing the defect density at the interface.

Energy level alignment analysis

In addition to the interaction effect, the electron-withdrawing Br-substitution serves to decrease the HOMO level of the SAMs, thereby enhancing energy level alignment with the perovskite layer. According to Gaussian calculations, **DCB-Br-2** has the lowest HOMO level of −5.45 eV (Fig. S14, ESI†), followed by **DCB-Br-1** (−5.34 eV) (Fig. S15, ESI†) and **DCB-C4POH** (−5.09 eV) (Fig. S16, ESI†). We conducted ultraviolet photoelectron spectroscopy (UPS) measurements to investigate the energy level alignment between SAMs and perovskites (Fig. 2a and Fig. S17, ESI†). The WFs of the ITO/SAMs are increased from 4.69 eV (**DCB-C4POH**) to 5.03 eV and 5.20 eV for **DCB-Br-1** and **DCB-Br-2**, respectively. And the WF of the WBG perovskite is 4.80 eV in Fig. S17 (ESI†). Combing their optical bandgaps (3.20 eV for **DCB-C4POH**, 3.06 eV for **DCB-Br-1**,

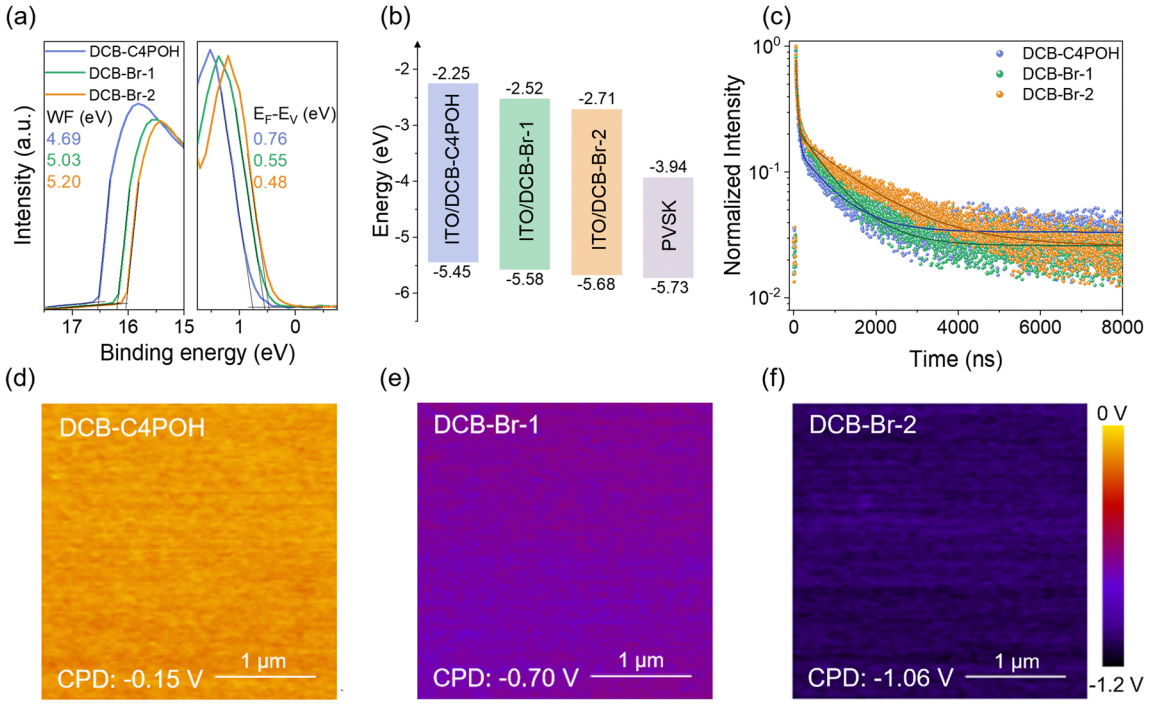

Fig. 2 Characteristics of SAMs and perovskite films deposited on SAMs. (a) UPS spectra of ITO/SAMs. (b) Energy level diagram of different ITO/SAMs and PVSK. (c) TRPL spectra of perovskite films deposited on ITO/SAMs. KPFM images of ITO/**DCB-C4POH** (d), ITO/**DCB-Br-1** (e), and ITO/**DCB-Br-2** (f).

3.13 eV for **DCB-Br-2**, and 1.785 eV for perovskite), as obtained from the absorption spectra in Fig. S18 and S19 (ESI†), we plotted the energy band structure of the different SAMs (Fig. 2b). ITO/**DCB-Br-2** exhibits the smallest valence band offset of 0.05 eV with perovskite, succeeded by ITO/**DCB-Br-1** at 0.15 eV, and ITO/**DCB-C4POH** at 0.28 eV. Therefore, **DCB-Br-2** could greatly reduce the energy level misalignment between the HTL and perovskite layer compared to **DCB-C4POH** and **DCB-Br-1**, facilitating faster hole extraction from the perovskite layer to the HTL. Furthermore, kelvin probe force microscopy (KPFM) measurements were conducted to evaluate the average surface contact potential difference (CPD) of different ITO/SAMs (Fig. 2d–f). The CPD values for ITO/**DCB-C4POH**, ITO/**DCB-Br-1**, and ITO/**DCB-Br-2** are −0.15 V, −0.70 V, and −1.06 V, respectively. The lower CPD of ITO/**DCB-Br-2** means a larger WF than the other two,[51,52] which is consistent with the UPS results. We then observed a faster hole extraction in the **DCB-Br-2** case, which can be confirmed by time-resolved photoluminescence (TRPL) measurements as shown in Fig. 2c and Table S1 (ESI†). For the **DCB-Br-2**-based sample, faster initial decay in the early times was discovered, showing a lower τ_1 value of 28.54 ns compared to the **DCB-Br-1**-based sample (33.36 ns) and **DCB-C4POH**-based sample (40.02 ns), indicating faster hole extraction from the perovskite layer to **DCB-Br-2**.[53–55] The τ_2 values of **DCB-Br-2** and **DCB-Br-1**-based samples are 1489.18 ns and 783.46 ns, respectively, higher than the **DCB-C4POH**-based sample of 776.19 ns. The longer τ_2 value indicates that the interfacial non-radiative recombination is effectively suppressed by **DCB-Br-2**,[12] which is consistent with the previous PL mapping results.

The introduction of bromine into the SAM not only enhances the surface interaction between the SAMs and perovskites but also lowers the HOMO level of the SAM, thereby improving energy level alignment. The position of the Br substitution plays a critical role in this enhancement. Specifically, **DCB-Br-2** exhibits reduced steric hindrance and higher electron density, enabling stronger interactions with the perovskite and more effective defect passivation. Furthermore, **DCB-Br-2** possesses a deeper work function, and the **DCB-Br-2**-modified ITO exhibits improved energy level alignment compared to **DCB-Br-1**. As a result, **DCB-Br-2** demonstrates superior performance over **DCB-Br-1** in terms of both surface interaction and energy level optimization.

Performance of wide-bandgap PSCs and V_{OC} loss analysis

Encouraged by the stronger interaction and better energy level alignment, we fabricated single-junction WBG perovskite solar cells with an inverted device structure of glass/ITO/SAMs/C_{60}/BCP/Ag. As shown in Fig. 3a and Fig. S20 (ESI†), the best performance was achieved by **DCB-Br-2**-based device with a remarkable V_{OC} of 1.37 V (1.36 V), a PCE of 20.76% (20.42%), an FF of 83.53% (83.15%), and a J_{SC} of 18.12 mA cm^{-2} (18.08 mA cm^{-2}) under reverse (forward) scan with negligible hysteresis. The device further demonstrated good operational stability, maintaining a stabilized PCE of 20.5% during 400 seconds of maximum power point (MPP) tracking (Fig. S21, ESI†). The performance of **DCB-Br-1** was slightly better than the control sample **DCB-C4POH** with a higher V_{OC} of 1.33 V, a PCE of 19.54%, an FF of 82.81%, and a J_{SC} of 17.70 mA cm^{-2} (V_{OC} = 1.31 V, PCE = 19.08%, FF = 82.31%, and J_{SC} = 17.64 mA cm^{-2} for **DCB-C4POH**). The integrated J_{SC} values obtained from external quantum efficiency (EQE) spectra for **DCB-C4POH**, **DCB-Br-1**, and **DCB-Br-2** are 17.18 mA cm^{-2}, 17.29 mA cm^{-2}, and 17.52 mA cm^{-2}, respectively (Fig. 3b), consistent with the J_{SC}s from the *JV*

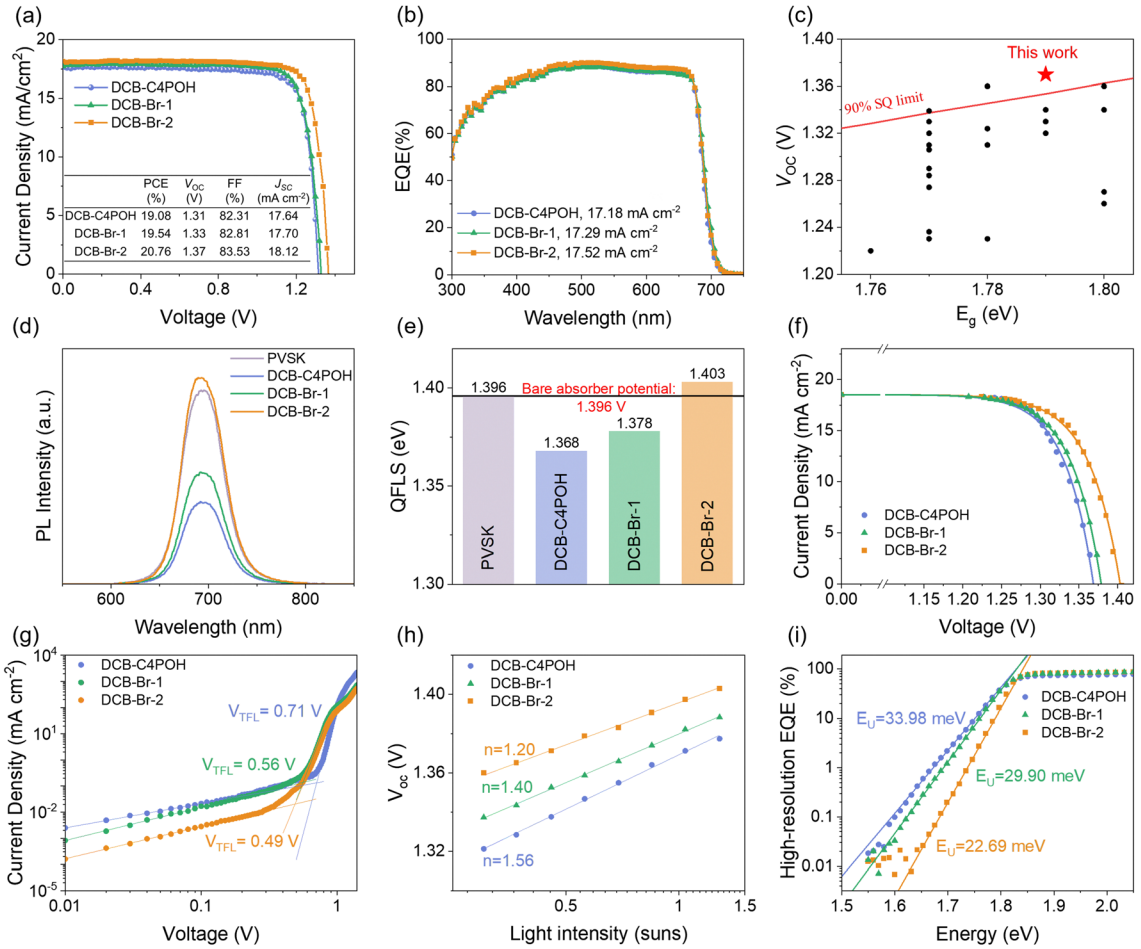

Fig. 3 Single-junction wide-bandgap solar cell performances and characterizations with different HTLs. (a) *JV* curves of WBG PSCs based on **DCB-C4POH**, **DCB-Br-1**, and **DCB-Br-2** with an aperture area of 0.055 cm^2. (b) EQE spectra of WBG PSCs with different HTLs, the integrated J_{SC} for **DCB-C4POH**, **DCB-Br-1**, and **DCB-Br-2** are 17.18, 17.29, and 17.52 mA cm^{-2}, respectively. (c) Summary of the reported V_{OC} values with bandgaps ranging from 1.76 to 1.80 eV (the detailed photovoltaic performance is presented in Table S2, ESI†). (d) Steady-state PL spectra of perovskite films on different substrates. Purple: glass/Al_2O_3/PVSK; blue: glass/Al_2O_3/**DCB-C4POH**/PVSK; green: glass/Al_2O_3/**DCB-Br-1**/PVSK; orange: glass/Al_2O_3/**DCB-Br-2**/PVSK. (e) The calculated QFLS values obtained from the steady-state PL measurements. (f) p-*JV* curves of perovskites with different HTLs as obtained from intensity-dependent PLQY measurements. (g) SCLC of the hole-only devices (glass/ITO/SAMs/perovskite/PTAA/MoO_X/Ag). (h) Light intensity-dependent V_{OC} of perovskites with different SAMs. (i) High-resolution EQE measurements of WBG PSCs with different HTLs.

measurements. And the 1st derivative of the EQE spectrum was also calculated to verify the bandgap, which is 1.79 eV (Fig. S22, ESI†). Similarly, the bandgaps obtained from UV-vis absorption (1.785 eV) and PL measurements (1.789 eV) align well with the EQE results, confirming their consistency. The overall performance is significantly enhanced by **DCB-Br-2**, as evidenced by increases in FF, J_{SC}, and particularly V_{OC}, which shows a remarkable improvement of 0.06 V compared to the controlled sample **DCB-C4POH**. The statistical distribution of the photovoltaic performance is shown in Fig. S23 (ESI†), demonstrating that the V_{OC} improvements of **DCB-Br-2** and **DCB-Br-1** compared to **DCB-C4POH** are reproducible with average V_{OC}s of 1.347 ± 0.012 V, 1.313 ± 0.013 V, and 1.300 ± 0.0134 V, respectively. Apart from the improvement in V_{OC}, the enhancement in FF is also notable, with an average FF of 80.06 ± 2.06%, significantly higher than that of **DCB-Br-1** (78.85 ± 2.70%) and **DCB-C4POH** (78.69 ± 3.32%). This increase in FF can be attributed to the effective passivation of interfacial defects and improved energy level alignment. Moreover, **DCB-Br-2**-based devices exhibit an increased J_{SC}, driven by the reduced interfacial non-radiative recombination and enhanced hole extraction.

Fig. 3c summarizes the reported V_{OC} values of WBG PSCs with a bandgap of 1.76 to 1.80 eV (the detailed data are presented in Table S2, ESI†). To the best of our knowledge, our champion V_{OC} of 1.37 V (bandgap: 1.79 eV) is among the highest values reported so far, surpassing 90% of S–Q limit with only 0.42 V V_{OC} loss.[56] Additionally, the nonradiative recombination V_{OC} loss is calculated to be 0.13 V. To better understand the origin of the improved V_{OC}, we performed steady-state photoluminescence (PL) and PL quantum yield (PLQY). As shown in Fig. 3d, the perovskite film on **DCB-Br-2** shows the strongest PL intensity, followed by perovskite film on **DCB-Br-1** and then on **DCB-C4POH**. Fig. 3e shows the calculated quasi-Fermi level splitting (QFLS) or implied V_{OC} of perovskite films

deposited on different SAMs. Perovskite film on **DCB-Br-2** shows the highest QFLS of 1.403 eV, which is even higher than the perovskite film itself (QFLS = 1.396 eV), followed by QFLSs of perovskites on **DCB-Br-1** and **DCB-C4POH**, which are 1.378 and 1.368 eV, respectively. The stronger PL intensity and QFLS of the perovskite film on **DCB-Br-2** compared to bare perovskite and perovskites on **DCB-C4POH** and **DCB-Br-1** suggests a reduction in non-radiative recombination due to enhanced defect passivation and accelerated hole extraction at the HTL/perovskite interface. We also constructed the pseudo-current–voltage (p-*JV*) curves (Fig. 3f) from intensity-dependent absolute PL measurements without transport loss, the detailed parameters are listed in Table S3 (ESI†). With **DCB-Br-2**, the drop of the pseudo-FF (p-FF) introduced by the HTL/perovskite interface is the lowest (from 91.4% to 88.8%), indicating the reduced non-radiative recombination loss and contributing to a higher device FF (Fig. S24, ESI†). With the increased pseudo-V_{OC} (p-V_{OC}) and p-FF, the achieved pseudo-PCE (p-PCE) for **DCB-Br-2**-based device is 22.95%, higher than that of **DCB-Br-1** (22.42%) and **DCB-C4POH** (22.24%) based devices. We further used the space charge limited current (SCLC) characterization to analyze the trap density level based on hole-only devices with the structure of glass/ITO/SAMs/perovskite/PTAA/MoO_X/Ag (Fig. 3g). The trap-filled limit voltage (V_{TFL}) value of **DCB-Br-2**-based device is the smallest (0.49 V), indicating the lowest trap density, likely due to the improved perovskite quality on the **DCB-Br-2** surface. The ideal factor (n), derived from the linear fitting of the intensity-dependent V_{OC} measurements, shows the value closest to 1 on **DCB-Br-2**-based device (the n values for **DCB-C4POH**, **DCB-Br-1**, and **DCB-Br-2**-based perovskite film are 1.56, 1.40, and 1.20, respectively), indicating a lowest Shockley-Read-Hall recombination in Fig. 3h. The Urbach energy values derived from high-resolution EQE measurements (Fig. 3i) decrease from 33.98 meV for **DCB-C4POH** to 29.90 meV and 22.69 meV for **DCB-Br-1** and **DCB-Br-2**, respectively. This suggests a decreased electronic disorder of the **DCB-Br-2**-based device, indicating reduced non-radiative recombination. Fig. S25 (ESI†) shows the *JV* curves of PSCs with different SAMs under the dark condition,

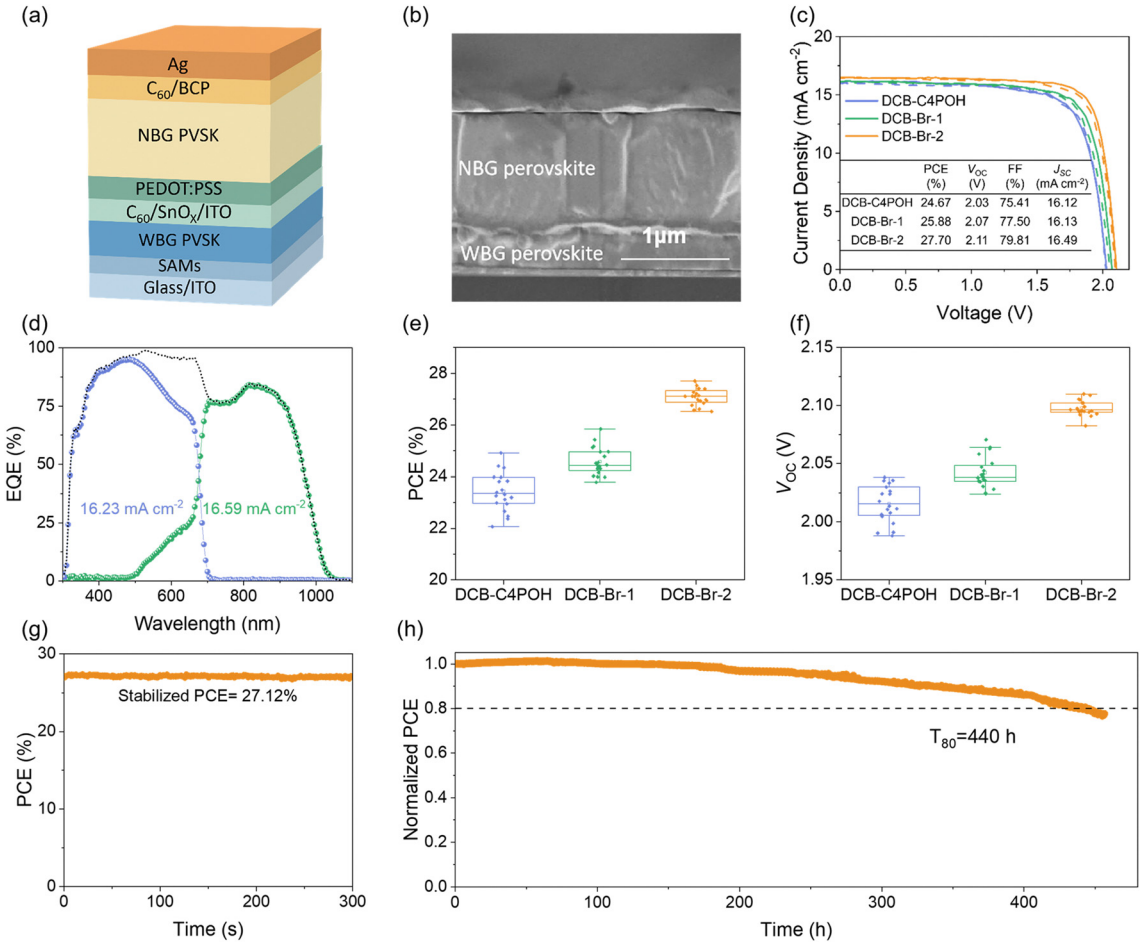

Fig. 4 All-perovskite TSC performances and characterizations with different HTLs. (a) Device configuration of the two-terminal all-perovskite TSC. (b) Cross-sectional SEM image of an all-perovskite TSC. (The WBG perovskite layer is ~370 nm thick, and the NBG layer is ~1100 nm). (c) *JV* curves of all-perovskite TSCs based on **DCB-C4POH**, **DCB-Br-1**, and **DCB-Br-2** with an aperture area of 0.055 cm^2 (solid line: reverse scan, dash line: forward scan, inset table are the photovoltaic parameters of the reverse scan). (d) EQE spectra of the TSC including the integrated J_{SC} values. Statistic PCE (e) and V_{OC} (f) distribution of TSCs with different HTLs (20 devices in count). (g) 5 min MPP tracking of the **DCB-Br-2**-based TSC (unencapsulated, 20 °C, in glovebox). (h) MPP tracking under continuous 1-sun illumination of the **DCB-Br-2**-based TSC (encapsulated, in ambient air, 25 °C, ~85% RH, ISOS-L-1).

the **DCB-Br-2**-based device shows the lowest dark current, indicating reduced current leakage. All the results substantiate that **DCB-Br-2** reduces the density of defect states and significantly suppresses the non-radiative recombination, which are consistent with the increased V_{OC} and FF in **DCB-Br-2**-based devices.

Performance of all-perovskite TSCs

To demonstrate the application potential of **DCB-Br-2** in TSCs, we integrated the optimized WBG top cell with the 1.25-eV NBG bottom cell. The NBG $Cs_{0.05}FA_{0.7}MA_{0.25}Pb_{0.5}Sn_{0.5}I_3$ subcell was optimized using ethane-1,2-diammonium iodide (EDAI) post-treatment. As shown in Fig. S26 (ESI†), EDAI treatment significantly enhanced the device performance, increasing the average PCE from 17.32 ± 0.89% to 19.44 ± 0.75%. The EDAI-treated NBG subcell achieved a champion PCE of 20.89%, with a V_{OC} of 0.804 V, an FF of 78.38%, and a J_{SC} of 33.14 mA cm^{-2} as shown in Fig. S27 (ESI†). Furthermore, the EQE spectrum of the NBG PSC (Fig. S27b, ESI†) shows an integrated J_{SC} of 32.62 mA cm^{-2}, which aligns well with the J_{SC} obtained from the *JV* measurement. The device structure of the TSC is glass/ITO/SAMs/WBG PVSK/C_{60}/SnO_x/ITO/PEDOT:PSS/NBG PVSK/C_{60}/BCP/Ag (Fig. 4a). We optimized the thickness of the WBG and NBG perovskite layers to achieve current matching between the two subcells. The optimized perovskite thicknesses are ∼370 nm for WBG perovskite and ∼1100 nm for NBG perovskite, as confirmed by the cross-sectional SEM image (Fig. 4b), which also demonstrates excellent crystallinity of the tandem stack. The *JV* curves of the tandem device with varying SAM HTLs are shown in Fig. 4c, the detailed parameters are listed in Table S4 (ESI†). The improvements of V_{OC} and FF are prominent in the **DCB-Br-2**-based TSC. The champion TSC based on **DCB-Br-2** exhibits a high PCE of 27.70% (V_{OC} = 2.11 V, FF = 79.81%, and J_{SC} = 16.49 mA cm^{-2}) under the reverse scan with negligible hysteresis. The EQE-integrated J_{SC} values for WBG and NBG subcells are 16.23 and 16.59 mA cm^{-2}, respectively (Fig. 4d), demonstrating a well-matched current and aligning closely with the J_{SC} values obtained from the *JV* measurement. Fig. 4e and f, and Fig. S28 (ESI†) show the statistical distribution of the photovoltaic parameters based on these three SAMs in the same batch. **DCB-Br-2**-based tandem devices show higher repetability with an averaged PCE and V_{OC} of 27.07 ± 0.32% and 2.097 ± 0.006 V, respectively. The improvement in V_{OC} achieved by **DCB-Br-2** is significant and reproducible, primarily due to the enhanced V_{OC} of the WBG subcell. However, the tandem devices experience an additional V_{OC} loss of approximately 0.05 V, attributed to the interconnection layer (ICL) and tandem fabrication processes. Addressing and minimizing these losses in the tandem stack will be a key focus of our future efforts. As shown in Fig. S28 (ESI†), the FF and J_{SC} improvements are also notable, driven by the better performance of the WBG subcell and its improved current matching with NBG subcell. Turning to device stability, the **DCB-Br-2**-based tandem solar cell demonstrated good performance, maintaining a steady-state efficiency of 27.12% after 300 seconds of MPP tracking (Fig. 4g). Furthermore, the encapsulated **DCB-Br-2**-based tandem device exhibited strong operational stability under the ISOS-L-1 protocol,[57] retaining 80% of its initial PCE after 440 hours of MPP tracking (Fig. 4h).

Conclusions

Through the utilization of the Br substitution strategy, we successfully created **DCB-Br-1** and **DCB-Br-2**. As revealed by XPS, Br substituents on the DCB terminal group have an interaction with the uncoordinated Pb^{2+}. We also found that different Br substitution positions can effectively manipulate the interaction strength between SAMs and perovskites. **DCB-Br-2**, with stronger interaction, suppresses interfacial defects more effectively and exhibits better energy level alignment. As a result, we achieved an impressive V_{OC} of up to 1.37 V with a PCE of 20.76% based on **DCB-Br-2**, which is among the highest reported V_{OC} values of WBG PSCs with similar bandgaps. Moreover, we demonstrated a two-terminal all-perovskite TSC with a champion efficiency of 27.70% by integrating it with a 1.25-eV NBG perovskite subcell. Our work highlights the significance of designing the SAM HTL through careful modification of the terminal group, paving the way for high-performance perovskite-based TSCs.

Author contributions

Conceptualization: Z. W., X. Y., and Y. H.; methodology: Z. W., Q. Z., and Y. H.; investigation: Z. W., Q. Z., S. L., Z. D., H. L., J. C., Z. S., X. W., Z. J., X. G., R. G., X. M., Y. W., Z. X., and Z. L.; formal analysis: Z. W., X. N., N. L., Y. H.; visualization: Z. W. and Y. H.; writing – original draft: Z. W.; writing review & editing: Z. W., X. N., Q. Z., X. Y., and Y. H.; resources: A. G. A., X. Y., and Y. H.; supervision: Y. H.; funding acquisition: A. G. A. and Y. H.; project administration: Y. H.

Data availability

The data supporting this article have been included as part of the ESI.†

Conflicts of interest

X. Y. has submitted a patent (CN116731069A) for the **DCB-Br-2** molecule described above and for their use in perovskite solar cells. Y. H. is the founder of Singfilm Solar, a company commercializing perovskite photovoltaics.

Acknowledgements

This work was financially supported by the Solar Energy Research Institute of Singapore (SERIS), a research institute at the National University of Singapore (NUS). SERIS is supported by NUS, the National Research Foundation Singapore (NRF), the Energy Market Authority of Singapore (EMA), and the Singapore Economic Development Board (EDB). X. Y. in acknowledges the financial support from China Postdoctoral

Science Foundation (No. 2021M702317) and Jiaxing Public Welfare Research Program (No. 2023AY40002).

References

1 M. A. Green, E. D. Dunlop, M. Yoshita, N. Kopidakis, K. Bothe, G. Siefer, D. Hinken, M. Rauer, J. Hohl-Ebinger and X. Hao, *Prog. Photovoltaics Res. Appl.*, 2024, **32**, 425–441.
2 M. C. Hanna and A. J. Nozik, *J. Appl. Phys.*, 2006, **100**, 074510.
3 A. W. Y. Ho-Baillie, J. Zheng, M. A. Mahmud, F.-J. Ma, D. R. McKenzie and M. A. Green, *Appl. Phys. Rev.*, 2021, **8**, 041307.
4 R. Lin, J. Xu, M. Wei, Y. Wang, Z. Qin, Z. Liu, J. Wu, K. Xiao, B. Chen, S. M. Park, G. Chen, H. R. Atapattu, K. R. Graham, J. Xu, J. Zhu, L. Li, C. Zhang, E. H. Sargent and H. Tan, *Nature*, 2022, **603**, 73–78.
5 S. Mahesh, J. M. Ball, R. D. J. Oliver, D. P. McMeekin, P. K. Nayak, M. B. Johnston and H. J. Snaith, *Energy Environ. Sci.*, 2020, **13**, 258–267.
6 J. Thiesbrummel, F. Peña-Camargo, K. O. Brinkmann, E. Gutierrez-Partida, F. Yang, J. Warby, S. Albrecht, D. Neher, T. Riedl, H. J. Snaith, M. Stolterfoht and F. Lang, *Adv. Energy Mater.*, 2022, **13**, 2202674.
7 H. Cui, L. Huang, S. Zhou, C. Wang, X. Hu, H. Guan, S. Wang, W. Shao, D. Pu, K. Dong, J. Zhou, P. Jia, W. Wang, C. Tao, W. Ke and G. Fang, *Energy Environ. Sci.*, 2023, **16**, 5992–6002.
8 H. Liu, J. Dong, P. Wang, B. Shi, Y. Zhao and X. Zhang, *Adv. Funct. Mater.*, 2023, **33**, 2303673.
9 L. Qiao, T. Ye, P. Wang, T. Wang, L. Zhang, R. Sun, W. Kong and X. Yang, *Adv. Funct. Mater.*, 2023, **34**, 2308908.
10 X. Shen, B. M. Gallant, P. Holzhey, J. A. Smith, K. A. Elmestekawy, Z. Yuan, P. V. G. M. Rathnayake, S. Bernardi, A. Dasgupta, E. Kasparavicius, T. Malinauskas, P. Caprioglio, O. Shargaieva, Y.-H. Lin, M. M. McCarthy, E. Unger, V. Getautis, A. Widmer-Cooper, L. M. Herz and H. J. Snaith, *Adv. Mater.*, 2023, **35**, 2211742.
11 Y. Zhao, C. Wang, T. Ma, L. Zhou, Z. Wu, H. Wang, C. Chen, Z. Yu, W. Sun, A. Wang, H. Huang, B. Zou, D. Zhao and X. Li, *Energy Environ. Sci.*, 2023, **16**, 2080–2089.
12 R. He, W. Wang, Z. Yi, F. Lang, C. Chen, J. Luo, J. Zhu, J. Thiesbrummel, S. Shah, K. Wei, Y. Luo, C. Wang, H. Lai, H. Huang, J. Zhou, B. Zou, X. Yin, S. Ren, X. Hao, L. Wu, J. Zhang, J. Zhang, M. Stolterfoht, F. Fu, W. Tang and D. Zhao, *Nature*, 2023, **618**, 80–86.
13 R. He, Z. Yi, Y. Luo, J. Luo, Q. Wei, H. Lai, H. Huang, B. Zou, G. Cui, W. Wang, C. Xiao, S. Ren, C. Chen, C. Wang, G. Xing, F. Fu and D. Zhao, *Adv. Sci.*, 2022, **9**, 2203210.
14 F. Yang, P. Tockhorn, A. Musiienko, F. Lang, D. Menzel, R. Macqueen, E. Kohnen, K. Xu, S. Mariotti, D. Mantione, L. Merten, A. Hinderhofer, B. Li, D. R. Wargulski, S. P. Harvey, J. Zhang, F. Scheler, S. Berwig, M. Ross, J. Thiesbrummel, A. Al-Ashouri, K. O. Brinkmann, T. Riedl, F. Schreiber, D. Abou-Ras, H. Snaith, D. Neher, L. Korte, M. Stolterfoht and S. Albrecht, *Adv. Mater.*, 2024, **36**, 2307743.
15 X. Zhou, H. Lai, T. Huang, C. Chen, Z. Xu, Y. Yang, S. Wu, X. Xiao, L. Chen, C. J. Brabec, Y. Mai and F. Guo, *ACS Energy Lett.*, 2023, **8**, 502–512.
16 Z. Yi, W. Wang, R. He, J. Zhu, W. Jiao, Y. Luo, Y. Xu, Y. Wang, Z. Zeng, K. Wei, J. Zhang, S.-W. Tsang, C. Chen, W. Tang and D. Zhao, *Energy Environ. Sci.*, 2024, **17**, 202–209.
17 J. Zhu, Y. Luo, R. He, C. Chen, Y. Wang, J. Luo, Z. Yi, J. Thiesbrummel, C. Wang, F. Lang, H. Lai, Y. Xu, J. Wang, Z. Zhang, W. Liang, G. Cui, S. Ren, X. Hao, H. Huang, Y. Wang, F. Yao, Q. Lin, L. Wu, J. Zhang, M. Stolterfoht, F. Fu and D. Zhao, *Nat. Energy*, 2023, **8**, 714–724.
18 J. Wen, Y. Zhao, P. Wu, Y. Liu, X. Zheng, R. Lin, S. Wan, K. Li, H. Luo, Y. Tian, L. Li and H. Tan, *Nat. Commun.*, 2023, **14**, 7118.
19 Z. Li, B. Li, X. Wu, S. A. Sheppard, S. Zhang, D. Gao, N. J. Long and Z. Zhu, *Science*, 2022, **376**, 416–420.
20 H. Chen, Q. Wei, M. I. Saidaminov, F. Wang, A. Johnston, Y. Hou, Z. Peng, K. Xu, W. Zhou, Z. Liu, L. Qiao, X. Wang, S. Xu, J. Li, R. Long, Y. Ke, E. H. Sargent and Z. Ning, *Adv. Mater.*, 2019, **31**, 1903559.
21 Z. Fang, N. Yan and S. F. Liu, *InfoMat*, 2022, **4**, e12369.
22 H. Bi, Y. Fujiwara, G. Kapil, D. Tavgeniene, Z. Zhang, L. Wang, C. Ding, S. R. Sahamir, A. K. Baranwal, Y. Sanehira, K. Takeshi, G. Shi, T. Bessho, H. Segawa, S. Grigalevicius, Q. Shen and S. Hayase, *Adv. Funct. Mater.*, 2023, **33**, 2300089.
23 H. Chen, A. Maxwell, C. Li, S. Teale, B. Chen, T. Zhu, E. Ugur, G. Harrison, L. Grater, J. Wang, Z. Wang, L. Zeng, S. M. Park, L. Chen, P. Serles, R. A. Awni, B. Subedi, X. Zheng, C. Xiao, N. J. Podraza, T. Filleter, C. Liu, Y. Yang, J. M. Luther, S. De Wolf, M. G. Kanatzidis, Y. Yan and E. H. Sargent, *Nature*, 2023, **613**, 676–681.
24 A. Al-Ashouri, E. Köhnen, B. Li, A. Magomedov, H. Hempel, P. Caprioglio, J. A. Márquez, A. B. Morales Vilches, E. Kasparavicius, J. A. Smith, N. Phung, D. Menzel, M. Grischek, L. Kegelmann, D. Skroblin, C. Gollwitzer, T. Malinauskas, M. Jošt, G. Matič, B. Rech, R. Schlatmann, M. Topič, L. Korte, A. Abate, B. Stannowski, D. Neher, M. Stolterfoht, T. Unold, V. Getautis and S. Albrecht, *Science*, 2020, **370**, 1300–1309.
25 A. Al-Ashouri, A. Magomedov, M. Roß, M. Jošt, M. Talaikis, G. Chistiakova, T. Bertram, J. A. Márquez, E. Köhnen, E. Kasparavičius, S. Levcenco, L. Gil-Escrig, C. J. Hages, R. Schlatmann, B. Rech, T. Malinauskas, T. Unold, C. A. Kaufmann, L. Korte, G. Niaura, V. Getautis and S. Albrecht, *Energy Environ. Sci.*, 2019, **12**, 3356–3369.
26 M. Li, M. Liu, F. Qi, F. R. Lin and A. K. Jen, *Chem. Rev.*, 2024, **124**, 2138–2204.
27 C. Duan, A. Tang, Q. Guo, W. Zhang, L. Yang, Y. Ding, Z. Dai and E. Zhou, *Adv. Funct. Mater.*, 2024, **34**, 2313462.
28 Y. Ding, C. Duan, Q. Guo, Y. Meng, Z. Wang, Z. Dai and E. Zhou, *Nano Today*, 2023, **53**, 102046.
29 Y. Ding, Q. Guo, Y. Geng, Z. Dai, Z. Wang, Z. Chen, Q. Guo, Z. Zheng, Y. Li and E. Zhou, *Nano Today*, 2022, **46**, 101586.

30 Q. Cheng, W. Chen, Y. Li and Y. Li, *Adv. Sci.*, 2024, **11**, 2307152.
31 S. Zhang, F. Ye, X. Wang, R. Chen, H. Zhang, L. Zhan, X. Jiang, Y. Li, X. Ji, S. Liu, M. Yu, F. Yu, Y. Zhang, R. Wu, Z. Liu, Z. Ning, D. Neher, L. Han, Y. Lin, H. Tian, W. Chen, M. Stolterfoht, L. Zhang, W.-H. Zhu and Y. Wu, *Science*, 2023, **380**, 404–409.
32 C. Li, Z. Zhang, H. Zhang, W. Yan, Y. Li, L. Liang, W. Yu, X. Yu, Y. Wang, Y. Yang, M. K. Nazeeruddin and P. Gao, *Angew. Chem., Int. Ed.*, 2024, **63**, e202315281.
33 G. Wang, J. Zheng, W. Duan, J. Yang, M. A. Mahmud, Q. Lian, S. Tang, C. Liao, J. Bing, J. Yi, T. L. Leung, X. Cui, H. Chen, F. Jiang, Y. Huang, A. Lambertz, M. Jankovec, M. Topič, S. Bremner, Y.-Z. Zhang, C. Cheng, K. Ding and A. Ho-Baillie, *Joule*, 2023, **7**, 2583–2594.
34 Z. Li, X. Sun, X. Zheng, B. Li, D. Gao, S. Zhang, X. Wu, S. Li, J. Gong, J. M. Luther, Z. A. Li and Z. Zhu, *Science*, 2023, **382**, 284–289.
35 W. Jiang, F. Li, M. Li, F. Qi, F. R. Lin and A. K. Y. Jen, *Angew. Chem., Int. Ed.*, 2022, **61**, e202213560.
36 A. Al-Ashouri, M. Marčinskas, E. Kasparavičius, T. Malinauskas, A. Palmstrom, V. Getautis, S. Albrecht, M. D. McGehee and A. Magomedov, *ACS Energy Lett.*, 2023, **8**, 898–900.
37 X. Zheng, Z. Li, Y. Zhang, M. Chen, T. Liu, C. Xiao, D. Gao, J. B. Patel, D. Kuciauskas, A. Magomedov, R. A. Scheidt, X. Wang, S. P. Harvey, Z. Dai, C. Zhang, D. Morales, H. Pruett, B. M. Wieliczka, A. R. Kirmani, N. P. Padture, K. R. Graham, Y. Yan, M. K. Nazeeruddin, M. D. McGehee, Z. Zhu and J. M. Luther, *Nat. Energy*, 2023, **8**, 462–472.
38 W. Wang, X. Liu, J. Wang, C. Chen, J. Yu, D. Zhao and W. Tang, *Adv. Energy Mater.*, 2023, **13**, 2300694.
39 A. Ullah, K. H. Park, Y. Lee, S. Park, A. B. Faheem, H. D. Nguyen, Y. Siddique, K.-K. Lee, Y. Jo, C.-H. Han, S. Ahn, I. Jeong, S. Cho, B. Kim, Y. S. Park and S. Hong, *Adv. Funct. Mater.*, 2022, **32**, 2208793.
40 A. Ullah, K. H. Park, H. D. Nguyen, Y. Siddique, S. F. A. Shah, H. Tran, S. Park, S. I. Lee, K.-K. Lee, C.-H. Han, K. Kim, S. Ahn, I. Jeong, Y. S. Park and S. Hong, *Adv. Energy Mater.*, 2022, **12**, 2270003.
41 X. Chen, C.-H. Chen, Z. H. Su, J. Chen, K.-L. Wang, Y. Xia, N. Nizamani, L. Huang, R.-J. Jin, Y.-H. Li, X. Yu Gao and Z.-K. Wang, *Adv. Funct. Mater.*, 2024, 2415004.
42 Z. Dai, S. You, D. Chakraborty, S. Li, Y. Zhang, A. Ranka, S. Barlow, J. J. Berry, S. R. Marder, P. Guo, Y. Qi, K. Zhu and N. P. Padture, *ACS Energy Lett.*, 2024, 1880–1887.
43 B. Chen, P. N. Rudd, S. Yang, Y. Yuan and J. Huang, *Chem. Soc. Rev.*, 2019, **48**, 3842–3867.
44 L. G. Bulusheva, A. V. Okotrub, E. Flahaut, I. P. Asanov, P. N. Gevko, V. O. Koroteev, Y. V. Fedoseeva, A. Yaya and C. P. Ewels, *Chem. Mater.*, 2012, **24**, 2708–2715.
45 Y. Zhou, Z. Wang, J. Jin, X. Zhang, J. Zou, F. Yao, Z. Zhu, X. Cui, D. Zhang, Y. Yu, C. Chen, D. Zhao, Q. Cao, Q. Lin and Q. Tai, *Angew. Chem., Int. Ed.*, 2023, **62**, e202300759.
46 V. R. Yandri, A. A. Nurunnizar, R. Debora, P. Wulandari, N. M. Nursam, R. Hidayat, E. D. Indari and Y. Yamashita, *Heliyon*, 2024, **10**, e23276.
47 S. Ning, S. Zhang, J. Sun, C. Li, J. Zheng, Y. M. Khalifa, S. Zhou, J. Cao and Y. Wu, *ACS Appl. Mater. Interfaces*, 2020, **12**, 43705–43713.
48 Q. Zhou, D. He, Q. Zhuang, B. Liu, R. Li, H. Li, Z. Zhang, H. Yang, P. Zhao, Y. He, Z. Zang and J. Chen, *Adv. Funct. Mater.*, 2022, **32**, 2205507.
49 M. Jeong, I. W. Choi, E. M. Go, Y. Cho, M. Kim, B. Lee, S. Jeong, Y. Jo, H. W. Choi, J. Lee, J.-H. Bae, S. K. Kwak, D. S. Kim and C. Yang, *Science*, 2020, **369**, 1615–1620.
50 C. Bi, Q. Wang, Y. Shao, Y. Yuan, Z. Xiao and J. Huang, *Nat. Commun.*, 2015, **6**, 7747.
51 Z. Zhang, R. Zhu, Y. Tang, Z. Su, S. Hu, X. Zhang, J. Zhang, J. Zhao, Y. Xue, X. Gao, G. Li, J. Pascual, A. Abate and M. Li, *Adv. Mater.*, 2024, **36**, e2312264.
52 F. Zhang, F. Ullrich, S. Silver, R. A. Kerner, B. P. Rand and A. Kahn, *J. Phys. Chem. Lett.*, 2019, **10**, 890–896.
53 D. Shi, V. Adinolfi, R. Comin, M. Yuan, E. Alarousu, A. Buin, Y. Chen, S. Hoogland, A. Rothenberger, K. Katsiev, Y. Losovyj, X. Zhang, P. A. Dowben, O. F. Mohammed, E. H. Sargent and O. M. Bakr, *Science*, 2015, **347**, 519–522.
54 X. Jiang, F. Wang, Q. Wei, H. Li, Y. Shang, W. Zhou, C. Wang, P. Cheng, Q. Chen, L. Chen and Z. Ning, *Nat. Commun.*, 2020, **11**, 1245.
55 M. Stolterfoht, C. M. Wolff, J. A. Márquez, S. Zhang, C. J. Hages, D. Rothhardt, S. Albrecht, P. L. Burn, P. Meredith, T. Unold and D. Neher, *Nat. Energy*, 2018, **3**, 847–854.
56 S. Rühle, *Sol. Energy*, 2016, **130**, 139–147.
57 M. V. Khenkin, E. A. Katz, A. Abate, G. Bardizza, J. J. Berry, C. Brabec, F. Brunetti, V. Bulović, Q. Burlingame, A. Di Carlo, R. Cheacharoen, Y.-B. Cheng, A. Colsmann, S. Cros, K. Domanski, M. Dusza, C. J. Fell, S. R. Forrest, Y. Galagan, D. Di Girolamo, M. Grätzel, A. Hagfeldt, E. von Hauff, H. Hoppe, J. Kettle, H. Köbler, M. S. Leite, S. Liu, Y.-L. Loo, J. M. Luther, C.-Q. Ma, M. Madsen, M. Manceau, M. Matheron, M. McGehee, R. Meitzner, M. K. Nazeeruddin, A. F. Nogueira, Ç. Odabaşı, A. Osherov, N.-G. Park, M. O. Reese, F. De Rossi, M. Saliba, U. S. Schubert, H. J. Snaith, S. D. Stranks, W. Tress, P. A. Troshin, V. Turkovic, S. Veenstra, I. Visoly-Fisher, A. Walsh, T. Watson, H. Xie, R. Yıldırım, S. M. Zakeeruddin, K. Zhu and M. Lira-Cantu, *Nat. Energy*, 2020, **5**, 35–49.